Bulletin of the Seismological Society of America, Vol. 109, No. 2, pp. 770–779, April 2019, doi: 10.1785/0120180150

Ⓔ

A Blind Thrust and Overlying Folding Earthquake of the 2016 M_w 6.0 Hutubi Earthquake in the Northern Tien Shan Fold-and-Thrust Belts, China

by Ying-Hui Yang, Jyr-Ching Hu, Qiang Chen, Ze-Gen Wang, and Min-Chien Tsai

Abstract The 2016 M_w 6.0 Hutubi earthquake occurred in the northern Tien Shan fold-and-thrust belts, China. However, the coseismic fault rupture model and the seismotectonics of the 2016 Hutubi earthquake remain uncertain up to the present due to the small magnitude, deep hypocenter, and no surface rupture caused by the seismogenic fault. Here, we show the evidence that the 2016 Hutubi earthquake occurred on a deep (15–20 km) blind-thrust fault, and the rupture of the blind fault triggers the slip of a shallow overlying fold. Ascending and descending Interferometric Synthetic Aperture Radar (InSAR) observations captured by Sentinel-1A/1B satellites are used to construct the seismogenic structure of the 2016 Hutubi earthquake. It is found that a single fault fails to provide a good fit to the observed Sentinel-1 ascending and descending InSAR deformation. A shallow fault-bend fold with strike along the surface trace of the Qigu anticline and a varying dip angle along the down-dip direction is proposed in this study based on the geodetic observations, which significantly improves the model fit to the InSAR observations. The estimated faulting model shows that the 2016 Hutubi earthquake occurred on a deep blind fault with 264.4° strike and 28.8° dip, and significant fault slip is located at the depth of 13–18 km with a peak slip of ~10.0 cm. The triggered shallow fault-bend fold has a listric surface with slight predominant thrust slip. The static Coulomb stress change from the mainshock on the shallow fold structure is negative, which indicates the dynamic stress may play a more important role than the static stress in the triggering of the shallow fault-bend fold in this case. The result of this study suggests that a moderate earthquake with a deep hypocenter has the potential to trigger the rupture of the shallow overlying fault-bend fold in this zone.

Electronic Supplement: Figures showing the Global Positioning System velocity field around 2016 Hutubi earthquake and aftershock distributions.

Introduction

On 8 September 2016, an earthquake with the magnitude of M_w 6.0 struck Hutubi County, Xinjiang Province, China, and the epicenter (43.823° N and 86.345° E of U.S. Geological Survey [USGS] solution) was located at ~56 km southeast of the city of Shihezi. This shock caused wall cracking of local structures in the Taxihe and Qingshuihe towns around the seismic zone, two injuries, and no fatality. The Hutubi earthquake occurred at the northern Tien Shan foreland basin, where long-term Global Positioning System observations indicate a shortening rate of ~23 mm/yr across the Tien Shan (Ⓔ Fig. S1, available in the electronic supplement to this article), which may accommodate ~50% of the shortening between the Indian and Eurasian plates (Yin *et al.*, 1998; Wang *et al.*, 2000, 2004, 2011; Dumitru *et al.*, 2001). Some of the strain accumulated across the northern Tien Shan fold-and-thrust belt was released during the Hutubi earthquake. The concept of fault-related folding can explain the evolution of folds in the upper-crustal levels, related to brittle processes (e.g., Suppe, 1983; Suppe *et al.*, 2004; Shaw *et al.*, 2005). Thus, it acts as an important coseismic deformation process (e.g., Kao and Chen, 2000; Chen *et al.*, 2001; Johnson and Segall, 2004; Guzofski *et al.*, 2007; Lu *et al.*, 2017).

The Qigu, Huoergous-Manas-Tugulu, and Dushanzi-Anjihai fold-and-thrust belts have developed along the margins between the northern Tien Shan and Junggar basin (Guan *et al.*, 2006, 2009; Yin, 2010). Previous studies show

Table 1
Parameters of Interferometric Pairs of Sentinel-1A/1B Synthetic Aperture Radar (SAR) Images

Sensor	Orbital Path (Number)	Slice Number	Acquisition Time (yyyy/mm/dd)	$B_\perp$ (m)	Heading Angle (°)	Incidence Angle (°)
Sentinel-1A	Ascending (114)	12	Master: 2016/11/19 Slave: 2016/12/13	−0.6	346	39.4
Sentinel-1B	Descending (92/3)	3	Master: 2016/11/24 Slave: 2017/12/18	125.4	194	33.6

"$B_\perp$" indicates the perpendicular baseline of the pair of SAR images.

that ~80 moderate earthquakes including three strong earthquakes (magnitude greater than **M** 7.0) have occurred in these fold-and-thrust belts since 1716 (Wang *et al.*, 2004; Lu *et al.*, 2018). The Hutubi earthquake is the largest seismic event recorded along the fold-and-thrust belts of northern Tien Shan in the past century (1916–2017). The largest on record is the 1906 **M** 7.7 Manas earthquake that occurred ~71 km west-northwest of the Hutubi event, and it was inferred that the Manas earthquake occurred at the Qingshuihe fault ramp beneath the northern Tien Shan, and whether the Hutubi earthquake and 1906 Manas earthquake share the same seismogenic fault still remains unknown (Xie and Cai, 1986; Zhang *et al.*, 1994; Zhou *et al.*, 2003; Wang *et al.*, 2004).

After the earthquake, USGS reported the estimated focal mechanism of the 2016 Hutubi earthquake is 80° for strike angle, 19° for the dip angle, and 81° for the rake angle, and the auxiliary nodal plane parameters are 269° for the strike angle, 71° for the dip angle, and 93° for the rake angle. Moreover, Liu *et al.* (2017) also inferred a source model of the Hutubi earthquake based on global teleseismic body waves. However, they concluded the teleseismic body waves used in the study did not yield a unique coseismic fault geometry because of the simple slip pattern and the insignificant directivity of the rupture extension. They infer that a north-dipping plane may be the seismogenic fault of the Hutubi event due to the good fit with the observed teleseismic body waveforms and good agreement with the distribution of aftershocks. However, the study by Lu *et al.* (2018), using the seismic reflection data, proposed a south-dipping reverse fault, which is considered as the seismogenic fault of both the 1906 Manas and 2017 Hutubi events. Both studies believe that the Hutubi earthquake does not cause apparent surface rupture due to the deep hypocenter and relatively small magnitude. The inconsistent results of the previous studies about the Hutubi earthquake make the source parameters uncertain, for example, the coseismic fault strike angle, dip angle, and slip distribution.

Here, we focus on both the seismogenic faulting model of the 2016 **M** 6.0 Hutubi earthquake and whether the main fault motion has triggered the rupture of the shallow overlying fault-bend fold structure. Previous studies show that some earthquakes, including the 1906 **M** 7.7 Manas earthquake (also occurred in northern Tien Shan fold-and-thrust belts), 1983 M_w 6.5 Coalinga earthquake, the 1985 Kettleman Hill earthquake, and the 1987 Whittier Narrows earthquake, occurring in fold-and-thrust belts share the same rupture pattern of a deep thrust fault and a shallow fold (King and Vita-Finzi, 1981; Stein and King, 1984; Zhang *et al.*, 1994; Yang *et al.*, 1998).

In this article, we first explore the activity of the shallow fault-bend fold based on the detailed geodetic Interferometric Synthetic Aperture Radar (InSAR) surface displacement fields. Then, we infer the likely seismogenic fault of the Hutubi event using the aftershocks distribution and a geological cross section. Furthermore, we infer the best-fit coseismic fault geometry and slip model using joint constraints of the Sentinel-1A ascending and Sentinel-1B descending InSAR observations, and discuss the relationship between the rupture of the shallow fault-bend fold and the activity of deep main fault. This study presents a detailed faulting model of the 2016 **M** 6.0 Hutubi earthquake and shows that a shallow fault-bend fold could be triggered by a moderate earthquake in the northern Tien Shan fold-and-thrust belts. In addition, we analyze the relationship of the seismogenic faults of the 2016 **M** 6.0 Hutubi and 1906 **M** 7.7 Manas events.

Data and Interpretation

We combined Sentinel-1A ascending and Sentinel-1B descending Synthetic Aperture Radar (SAR) data to measure the coseismic surface displacement fields of the Hutubi earthquake. Table 1 presents the detailed information of the used SAR data, and the coverage of the two tracks is shown in Figure 1. Obviously, both tracks cover the seismic area and the three fold-and-thrust zones in the piedmont of northern Tien Shan.

The ascending and descending Sentinel-1 C-band SAR images, acquired in the Terrain Observation with Progressive Scan (TOPS) imaging mode, are processed using the GAMMA InSAR software (Wegnuller *et al.*, 2016). To avoid the phase jumps in the overlapping area between the adjacent bursts of the TOPS SAR data, azimuth coregistration is repeatedly carried out (three times here) to acquire an azimuth alignment with the precision of 0.0001 pixel. The Shuttle Radar Topography Mission 4 digital elevation model is used to remove the topographic phase component (Farr *et al.*, 2007); and the minimum cost function algorithm is used to unwrap the InSAR interferograms (Wegnuller *et al.*, 2016). The high-coherence InSAR observations in the far field are used to estimate a 2D ramp that is removed from the initial unwrapped phase data to mitigate the orbital error (Huang *et al.*, 2016; Yang *et al.*, 2017). Figure 2 shows the InSAR

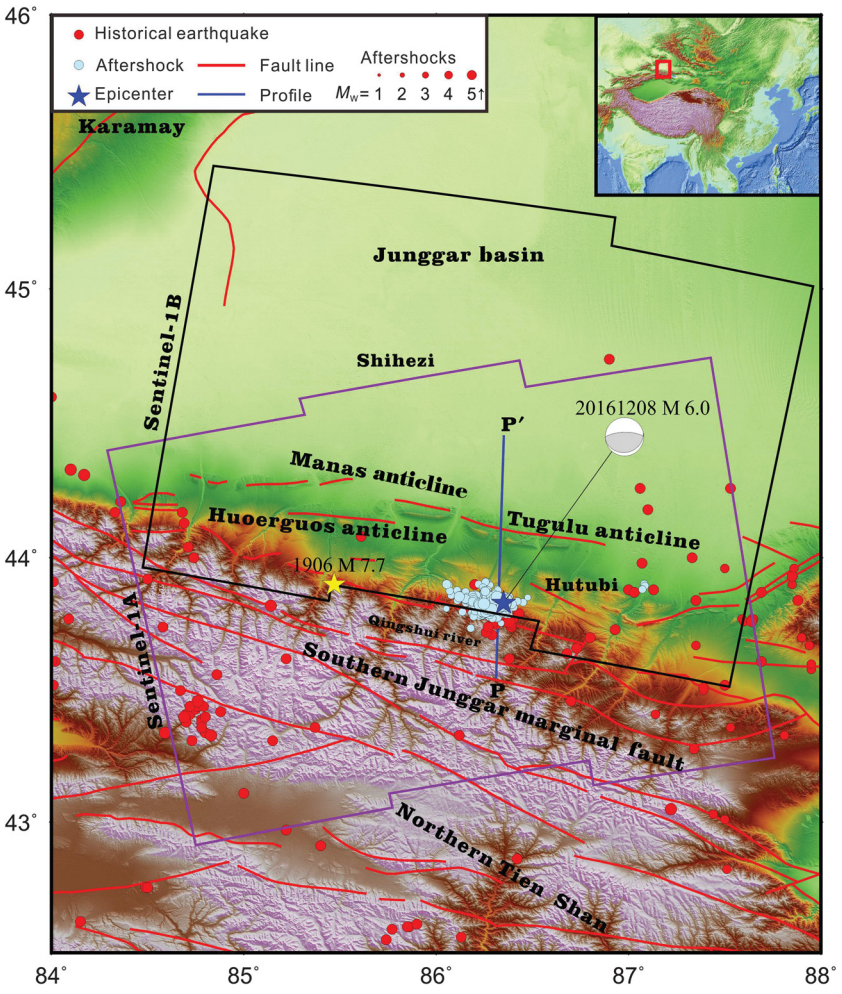

Figure 1. Map of the study region. Faults (red lines), historical earthquakes (red circles), and aftershocks (cyan circles) are mapped on shaded relief of Shuttle Radar Topography Mission 4 digital elevation model. Violet and black solid polygons indicate the footprint of Sentinel-1A ascending and Sentinel-1B descending tracks, respectively. The blue solid line indicates the surface trace of the seismic reflection section. Blue and yellow stars indicate the epicenters of the 2016 Hutubi earthquake and 1906 Manas earthquake, respectively.

deformation of the 2016 Hutubi earthquake. The Sentinel-1 ascending and descending data maintain interferometric coherence in the main seismic zone. The interferometric decorrelation in the south of the deformation fields could be caused by dense vegetation cover.

Both of the ascending and descending InSAR present positive deformation signals (shortening along the line-of-sight direction) in the seismic zone, which indicates that the surface displacements could be mainly controlled by the uplift motion. It suggests that the measured InSAR deformation has resulted from a predominant reverse event. High spatial resolution InSAR data provide the opportunity to map the fine surface movement in the main seismic zone. The sharp phase jumps and interferometric decorrelation can be found in the Sentinel-1 ascending and descending observations along the surface rupture trace marked by black arrows and dashed lines in Figure 2 and Ⓔ Figure S3. These cannot be caused by a single main fault rupture in the deep crust. In addition, the optimal image (Ⓔ Fig. S3) of this zone shows that there is a significant fold scarp along the trace of the phase jumps and interferometric decorrelation. Therefore, we hypothesize that a shallow fault rupture also contributes to the observed InSAR surface deformation fields.

Figure 3 and Ⓔ Figure S2 show the aftershocks distribution along the two cross sections of A–A′ and B–B′ (Lu *et al.*, 2018). The time-series distribution of aftershocks indicates that more than 63% aftershocks occurred in the four days after the mainshock. However, the large aftershocks with magnitudes more than **M** 4.0 were mainly concentrated in the 6–12 days period after the mainshock, and they could be triggered by the mainshock and/or the previous dense small aftershocks. The time-series aftershocks distribution on section A–A′ shows that dense aftershocks occurred around a north-dipping plane (the black solid line in Fig. 3 and Ⓔ Fig. S2) with a dip angle of ~30°, we hypothesize that this north-dipping plane may be the seismogenic fault responsible for the 2016 Hutubi earthquake (Lu *et al.*, 2018). The B–B′ section shows most of the aftershocks are located at the west of the epicenter, but few are found in the east of the epicenter. This suggests a single westward rupture propagation of the 2016 Hutubi earthquake.

Figure 4 shows the geologic profile across the surface trace of P–P′ (the blue solid line in Fig. 1) inferred from the seismic reflection data (Lu *et al.*, 2018). We can find from Figure 4 that fold-and-thrust belts have developed in the northern Tien Shan foreland basin. White circles indicating the aftershocks suggest a north-dipping seismogenic fault plane; however, no north-dipping fault has been interpreted in this zone. Therefore, we hypothesize that the mainshock of the Hutubi earthquake occurred on a blind north-dipping fault at depths of 8–20 km. Moreover, we suggest that the shallow fault-bend fold could be responsible for the sharp surface deformation observed by Sentinel-1 ascending and descending tracks. However, the multilayer overlying fault-bend folds at different depths make it difficult to distinguish which one has been triggered by the mainshock.

Method of Multifault Rupture Inversion

The original ascending and descending InSAR deformation fields are first downsampled using the quadtree algorithm to reduce the computational effort (Welstead, 1999).

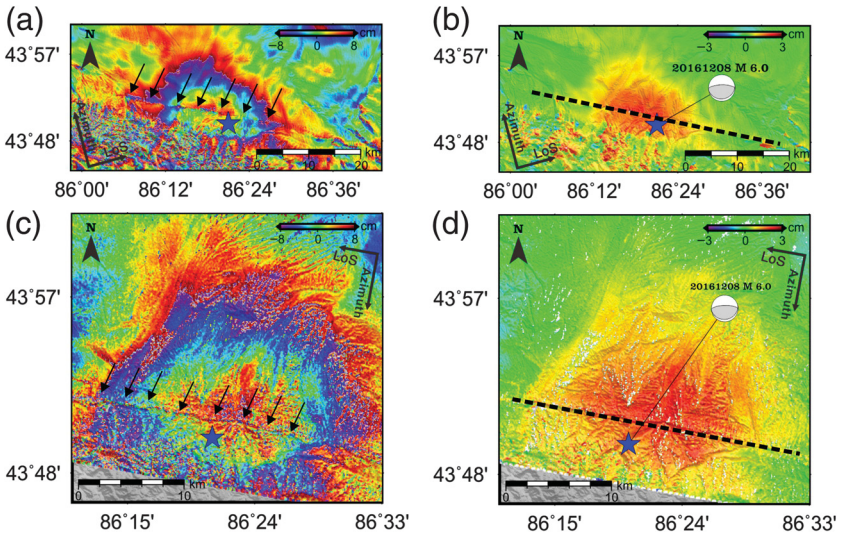

Figure 2. The Sentinel-1 Interferometric Synthetic Aperture Radar (InSAR) results. (a) The Sentinel-1A ascending InSAR interferogram and (c) deformation field of the 2016 Hutubi earthquake. (b) The unwrapped Sentinel-1B descending InSAR interferogram and (d) line-of-sight (LoS) deformation field of the 2016 Hutubi earthquake. Black arrows and the black dashed lines indicate the surface rupture trace of the triggered shallow fault, and blue stars denote the epicenter (U.S. Geological Survey [USGS] solution) of the Hutubi earthquake.

We preserve high coherence (>0.3) samples in the main seismic zone, and a total of 1261 points from the ascending and 1427 points from the descending InSAR observations are used to estimate the geometry and slip models of the main fault and the triggered shallow fault-bend folding of the 2016 Hutubi earthquake.

A north-dipping plane is preliminarily constructed to describe the main fault of the Hutubi earthquake. The main fault geometry parameters of the strike angle, dip angle, and source depth are set with bounds of [260°, 275°], [5°, 80°], and [−20 km, −5 km], respectively, based on the USGS solution. The strike angle of 278.4° and a length of 30 km of the shallow fault-bend fold are extracted from the surface rupture trace shown in Figure 2. Moreover, concerning fault-related folding in the northern Tien Shan zone, a listric fault composed of three subsegments with independent dip angles and widths along the down-dip direction is constructed to describe the triggered shallow fault-bend fold. The three subfault dip angle bounds are set as [0°, 90°], [0°, 90°], and [0°, 60°], respectively, considering the listric shape of the shallow fault-bend fold, and all the subfault widths share the same bounds of [0 km, 20 km].

We discretize the two faults with a size of 4 km × 4 km and estimate the optimal fault geometry parameters under the constraints of the Sentinel-1 ascending and descending

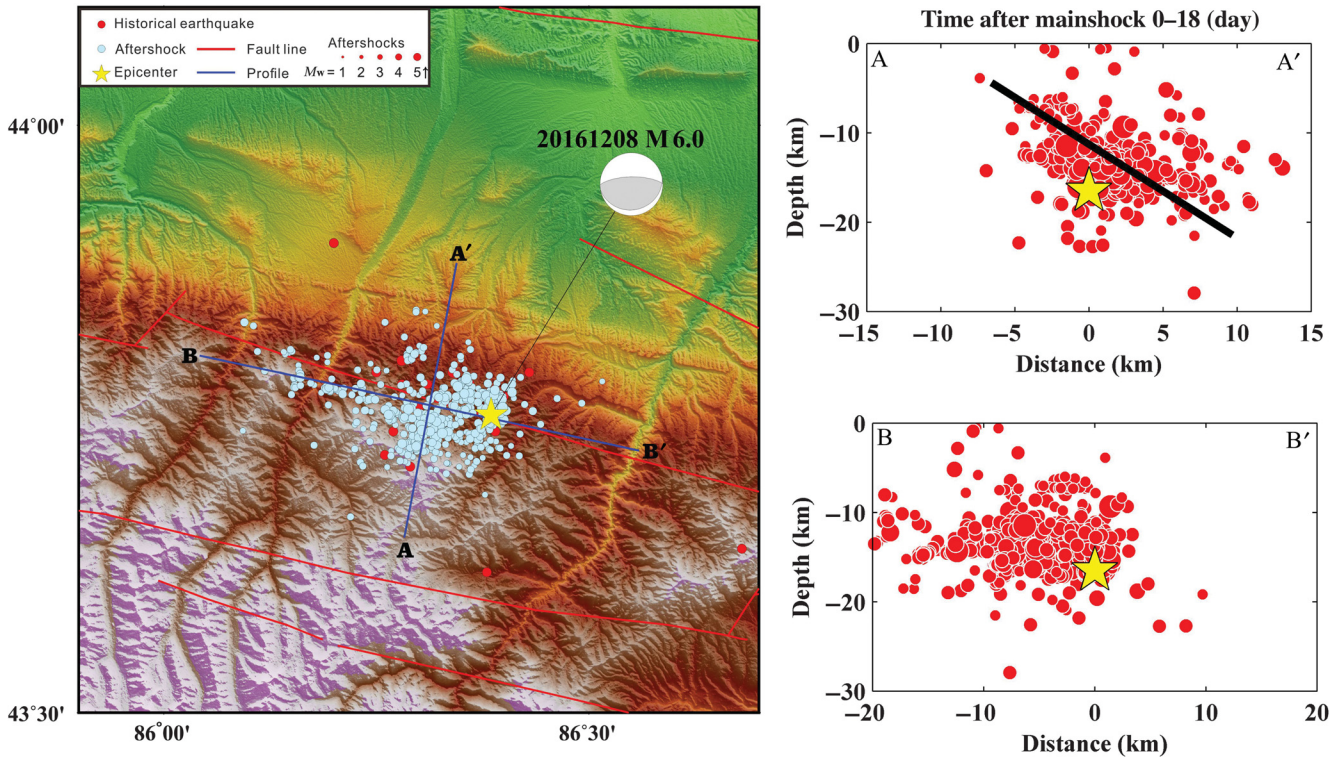

Figure 3. The aftershock distribution along two cross sections. Blue solid lines denote the two cross sections. Yellow stars are the epicenter in map view and hypocenter on the cross sections. Black solid line in A–A′ cross section indicates the predicted seismogenic fault of the 2016 Hutubi event based on the aftershocks distribution.

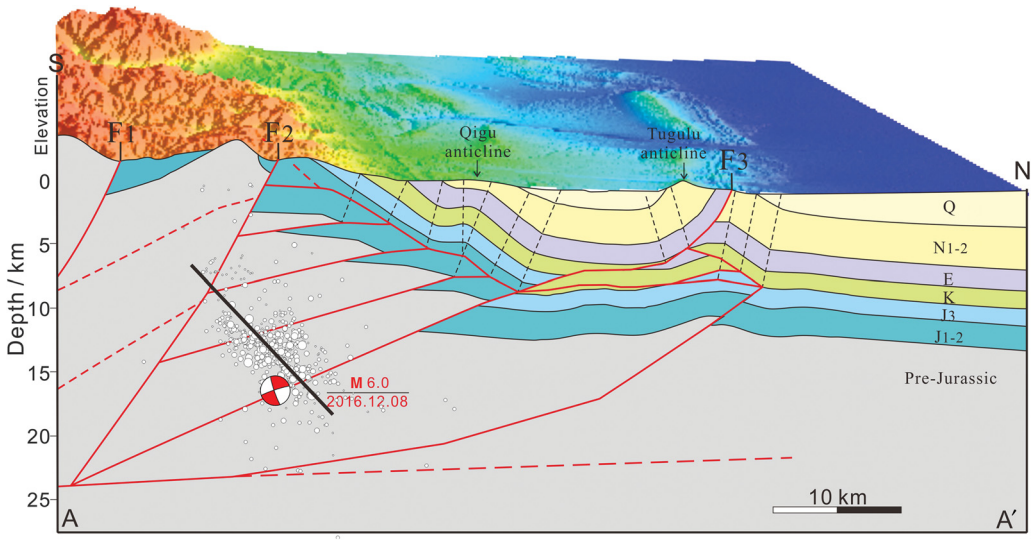

Figure 4. Geologic cross section of the trace of P–P′ (Fig. 1) interpreted from seismic reflection data, which is modified from the study by Lu *et al.* (2018). Solid lines indicate the interpreted faults, and dashed lines denote the axial surfaces. White circles are the aftershocks of the Hutubi earthquake, and the black solid line within the aftershocks denotes the possible seismogenic fault.

InSAR observations with equal weights. To avoid unphysical slip on the fault, Laplace smoothing constraints between adjacent fault patches are included into the inversion. Moreover, the inversion is further constrained with insignificant slip on the fault edges. The detailed inversion algorithm and processing including the estimation of the smoothing factor, fault geometry, and slip parameters can be found in our previous studies (Yang *et al.*, 2017; Yang, Chen, *et al.*, 2018; Yang, Tsai, *et al.*, 2018). Finally, the simulated annealing algorithm is used to train the parameters including the strike angle, dip angle and source depth of the main fault, and dip angles and widths of the subfaults of the shallow fault-bend folding until we get the best-fit parameters, which provide the globally maximum explained ratio (defined in the study by Yang, Tsai, *et al.*, 2018). Then, we fix the fault geometry and rediscretize the two faults using a small size of 1 km × 1 km to estimate the detailed slip distribution based on the finite rectangular dislocations in a homogeneous elastic half-space (Okada, 1985).

The fault proposed by Lu *et al.* (2018) shares the similar fault geometry with the conjugate fault suggested by the geologic cross section. The north-dipping fault is the most significant difference between the fault used in this study with the south-dipping fault proposed by Lu *et al.* (2018) who suggested a south-dipping ramp-flat-ramp structure might be the seismogenic fault of 2016 M_w 6.2 Hutubi and 1906 **M** 7.7 Manas earthquakes. However, Lu *et al.* (2018) also suggest an alternative seismogenic fault could be a north-dipping back thrust as a minor splay fault in the duplex of the structural wedge. Here, we also try to estimate the optimal faulting model under the assumption of the conjugate fault geometry (south dipping). The best-fitting south-dipping faulting model explains ∼83%, ∼81% ascending and descending InSAR observation. However, the explained ratios derived from the north-dipping fault are ∼94%, ∼97% of the ascending and descending InSAR data, both of which are higher than the results of the conjugate south-dipping fault. The study proposed by Liu *et al.* (2017) using teleseismic data also suggested that a north-dipping reverse fault should be responsible for the 2016 Hutubi earthquake. In addition, the north-dipping fault has a higher spatial consistency with the aftershocks than those of the south-dipping fault. Therefore, it is believed that the estimated north-dipping fault should be the seismogenic fault of the 2016 Hutubi earthquake.

Results

The inferred fault model suggests that the main blind fault of the Hutubi earthquake is a north-dipping fault plane with 264.4° strike and 28.8° dip located beneath the observed lobes of the InSAR deformation, in agreement with the previous teleseismic body-wave solution (Liu *et al.*, 2017). The estimated fault strike angle of 264.4° is similar to 269° of the USGS solution. However, the estimated dip angle of 28.8° in this study is less than 71° of the USGS solution, which should be due to the different constraint data (the USGS and our solutions are solved based on seismic waveform data and InSAR data, respectively). The inferred main fault-slip model (Fig. 5 and Ⓔ Fig. S4) shows a single major slip asperity at depths of 13–18 km with a peak slip of ∼10.0 cm, and the faulting is controlled by the predominant thrust motion with slight right-lateral strike-slip component. A slight slip zone controlled by the thrust motion with an average magnitude of ∼5.0 cm is found on the main blind fault at depths of 8–13 km, which suggests that the fault rupture has propagated to the shallow fault patches from the hypocenter. The seismic moment of the main fault is 8.2×10^{17} N · m, corresponding to an M_w 5.9 earthquake.

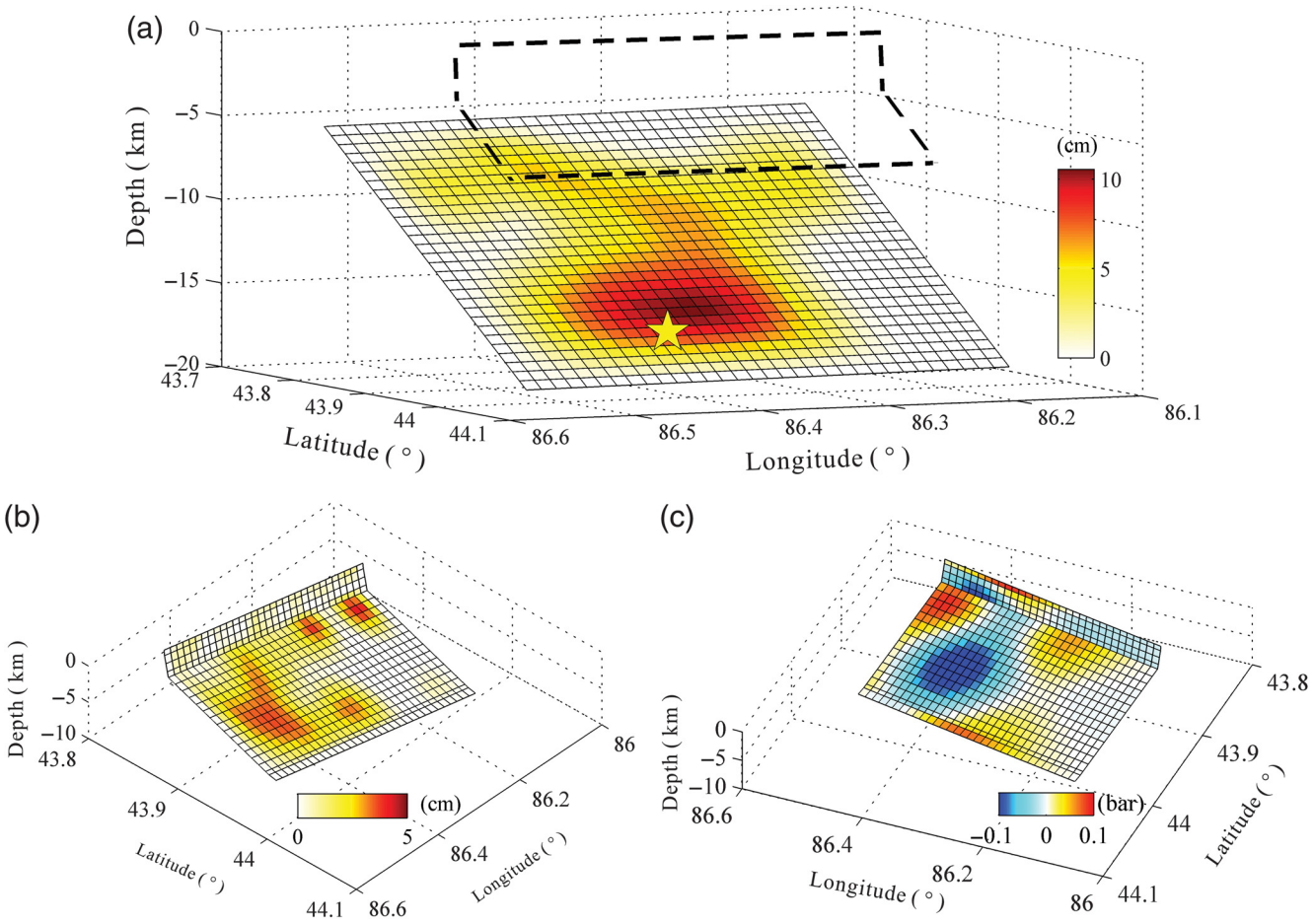

Figure 5. The best-fit faulting model inferred from joint InSAR ascending and descending observations. Map view of the slip distribution on (a) the main fault and (b) the triggered shallow fault. The yellow star is the hypocenter, black dashed lines denote the location of the shallow fault, and the color changing from white to red represents the magnitude of slip on the fault patches. (c) The static Coulomb stress on the shallow fault caused by the slip of the main fault.

The best-fit solution shows that the triggered shallow fault has a ramp-flat listric shape. The first subfault segment has a steep dip of 84.4° and width of 0.7 km, and it reaches to the surface with some slight slip. The adjacent second subfault segment has a similar steep dip of 78.8° and width of 2.7 km. The third subfault segment has a relatively lower dip angle of 15.2° but larger width of 15.2 km than the upper two segments, and significant slip has been found on the third subfault segment at the depth of 3–7 km. The shallow fault slip releases a seismic moment of 2.1×10^{17} N · m, corresponding to an M_w 5.5 earthquake. One large and two small slip asperity zones can be well separated from the slip model of the triggered shallow fault (Fig. 5 and Ⓔ Fig. S4). The major slip asperity zone with the size of 19×12 km^2 is located at the middle and east of the third subfault and has predominant thrust and slight left strike-slip components with a peak slip of ~3.5 cm at the depth of ~4.5 km. The two small slip asperity zones (the size less than 4×4 km^2) are mainly controlled by the thrust motion, but with different strike-slip motions (slight left-lateral strike slip for the east one and slight right-lateral strike slip for the west one). They are located at the west of the third subfault at a depth of 3.4–4.5 km, and the slip averages are ~2.2 cm of both two asperity zones.

We estimate the predicted Sentinel-1A ascending (Fig. 6b) and Sentinel-1B descending (Fig. 6h) InSAR deformation based on the main fault-slip model, and get the residuals (Fig. 6c,i) between the observations and predictions. We find that the main fault model has a predominant contribution to the observed InSAR deformation, and sharp residuals (indicated by the black arrows) are only concentrated in the north of the surface trace marked by red dashed lines. Figure 6d,j shows that the predicted InSAR deformation by the shallow fault model has good agreement with the residuals of the main fault model. None of sharp deformation remains in both the last ascending (Fig. 6e) and last descending (Fig. 6k) residuals. Small residuals shown in Figure 6e,k could be resulted from a combined contribution of the interferometric decorrelation (especially for the area in the southwest of ascending InSAR), atmospheric delay error, and surface displacements caused by the aftershocks. Figure 6f,l shows the integrated surface displacement fields

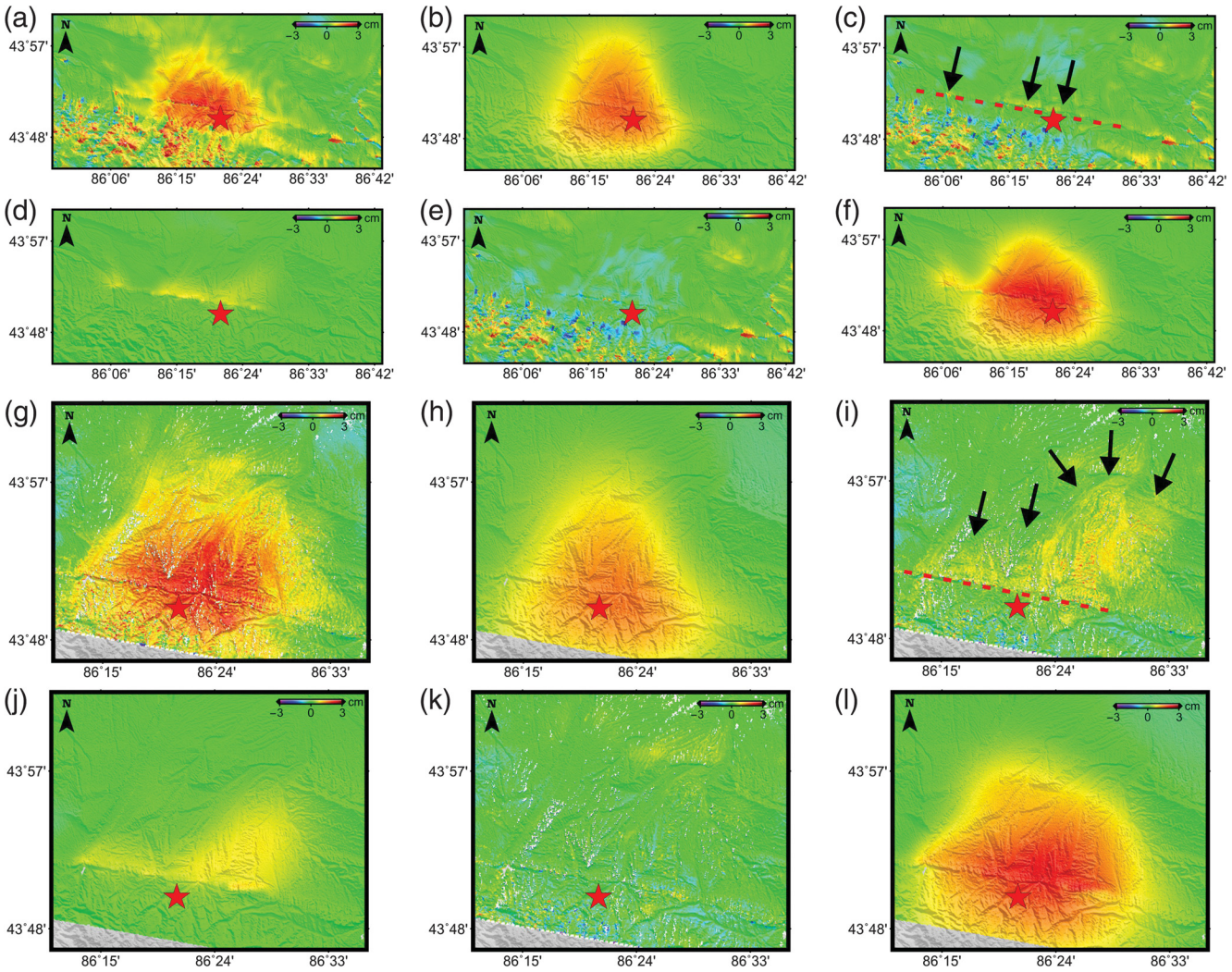

Figure 6. The observed, predicted, and residual Sentinel-1 InSAR deformations of the Hutubi earthquake. Red stars indicate the epicenter of the mainshock, and red dashed lines denote the surface rupture trace of the shallow fault triggered by the rupture of the blind main fault. Black arrows denote the sharp residuals after removal of the contribution of the main fault model, and they result from the activity of the triggered shallow fault. The observed (a) ascending and (g) descending Sentinel-1 InSAR deformation. The predicted (b) ascending and (h) descending Sentinel-1 InSAR deformation based on the main faulting model. The residual (c) ascending and (i) descending Sentinel-1 InSAR deformation after removed the contribution caused by the main fault. The predicted (d) ascending and (j) descending Sentinel-1 InSAR deformation based on the shallow faulting model. The residual (e) ascending and (k) descending Sentinel-1 InSAR deformation after removed the contribution caused by the shallow fault. The predicted (f) ascending and (l) descending InSAR deformation fields derived from both the main and the shallow faulting models.

of ascending and descending InSAR tracks, both of which have good agreement with the original observations.

To understand the stress transferring from the main fault to the shallow fault, we calculate the static Coulomb failure stress (CFS) change on the shallow fault using the main fault model as input source (Chen *et al.*, 2015). Figure 5c shows that the CFS change is positive at the two small slip asperities, but it decreases to ~0.1 bar at the major slip asperity of the shallow fault. It suggests that the rupture of the major slip asperity of the shallow fault is not triggered by the static CFS change from the main fault slip. Therefore, we hypothesize the dynamic CFS change may play a more important role than static CFS change in triggering the rupture of the shallow fault-bend fold of the Hutubi earthquake in agreement with the previous studies (Freed, 2005; Nissen *et al.*, 2016; Ishibe *et al.*, 2017).

Discussion and Conclusions

Indeed, by projecting the inferred deep main fault and triggered shallow fault along the geologic structure section (Fig. 7), we find good agreement between the triggered shallow fault and the interpreted fold and thrust in the shallow crust. The mainshock occurred on a deep blind-thrust fault; however, it is a little far away from the relocated aftershocks (marked by white circles), but nearer to the hypocenter of USGS solution. If we move the aftershocks based on location difference between the mainshocks solved by Lu *et al.* (2018)

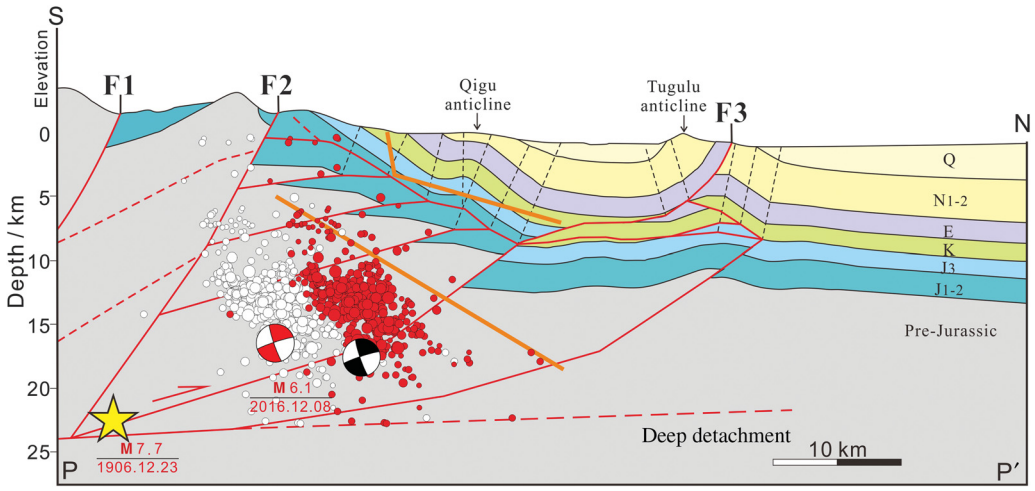

Figure 7. Geologic cross section of the trace of P–P′, which is modified from the study by Lu *et al.* (2018). Brown solid lines indicate the inferred seismogenic fault of the 2016 Hutubi earthquake. The yellow star is the hypocenter of the 1906 Manas earthquake. White circles are the relocated aftershocks, and red circles indicate the aftershocks after adjusted the location based on the coordinate difference between the mainshocks solved by Lu *et al.* (2018) and USGS.

and USGS, and the inferred main fault (marked by the brown line) obviously has better agreement with the aftershocks (marked by red circles). Therefore, we hypothesize that the disagreement between our inferred main fault and the aftershocks could be resulted from the inaccurate locations of the aftershocks.

The 1906 Manas **M** 7.7 earthquake occurred at the southwest of Hutubi event. Previous study proposed that the 1906 Manas earthquake caused by the rupture of F3 (Fig. 7), which is characterized by east–west trending and south dipping (Lu *et al.*, 2018). Opposite faults dipping suggest that the Hutubi earthquake and adjacent Manas earthquake have different seismogenic faults. Whether the 1906 **M** 7.7 Manas event has a positive triggering effect on the 2016 **M** 6.0 Hutubi earthquake needs further study. The studies by Zhang *et al.* (1994) and Yang *et al.* (1998) propose that the 1906 Manas earthquake occurred on the deep blind fault, and the coseismic rupture of the deep blind fault has triggered the motion of the shallow folds. In addition, the **M** 7.7 Manas earthquake reproduced the surface ruptures with offsets between 0.2 and 0.5 m in the Huoerguosi–Manas–Tugulu thrust-related anticline zones (Zhang *et al.*, 1994). It suggests that both the 2016 Hutubi and the 1906 Manas events are the blind thrust and overlying folding earthquakes.

Previous studies proposed that fold earthquakes could occur in the northern Tien Shan fold-and-thrust belts (Zhang *et al.*, 1994; Yang *et al.*, 1998). However, this is the first time that we have clear evidence from the surface displacements and inferred faulting model, both of which show that a blind-thrust fault and fold earthquake occurred in this fold-and-thrust belt. These events with deep blind-thrust fault and fault-related folding suggest that we should pay more attention to the shallow folds within the active fold and thrust belts because these shallow folds can possibly be triggered by strong or moderate earthquakes on deeper faults. In some cases this could cause a more severe threat than the mainshock.

Data and Resources

Sentinel-1A Synthetic Aperture Radar (SAR) images were provided by the European Space Agency (ESA) and were processed by the GAMMA software (Wegmueller and Werner, 1997). The U.S. Geological Survey (USGS) solution of the 2016 Hutubi earthquake can be found at https://earthquake.usgs.gov/earthquakes/eventpage/us20007z2r#moment-tensor (last accessed March 2018). Shuttle Radar Topography Mission (SRTM) digital elevation model data are the void-filled seamless SRTM data V4, available from the CGIAR-CSI SRTM 90 Database (http://srtm.csi.cgiar.org/, last accessed December 2017). The relocated aftershocks are solved by Lu *et al.* (2018). Figures were generated using the Generic Mapping Tools (GMT) software (Wessel and Smith, 1998).

Acknowledgments

The comments and suggestions from two anonymous reviewers and Associate Editor Ronni Grapenthin are deeply appreciated, which largely improve this article. The authors are deeply grateful for fruitful discussions to Renqi Lu, Xiwei Xu, and Zhe Su. Appreciation is also owed to Hsiu-Fang Lee, who helped us in preparing some figures. This work is supported by the National Key R&D Program of China (2017YFB0502700), the Ministry of Science and Technology in Taiwan under the Grants 105-2811-M-002-053 for the Cooperation in Seismology of Two Sides across Taiwan Strait and National Natural Science Foundation of China (Number 41472255). The authors thank Renqi Lu for providing the geologic cross section and aftershocks data.

References

Chen, Q., Y. Yang, R. Luo, G. Liu, and K. Zhang (2015). Deep coseismic slip of the 2008 Wenchuan earthquake inferred from joint inversion of

fault stress changes and GPS surface displacements, *J. Geodyn.* **87,** 1–12, doi: 10.1016/j.jog.2015.03.001.

Chen, W.-S., B.-S. Huang, Y.-G. Chen, Y.-H. Lee, C.-N. Yang, C.-H. Lo, H.-C. Chang, Q.-C. Sung, N.-W. Huang, C.-C. Lin, *et al.* (2001). 1999 Chi-Chi earthquake: A case study on the role of thrust-ramp structures for generating earthquakes, *Bull. Seismol. Soc. Am.* **91,** 986–994, doi: 10.1785/0120000731.

Dumitru, T. A., D. Zhou, E. Z. Chang, S. A. Graham, M. S. Hendrix, E. R. Sobel, and A. R. Carroll (2001). Uplift, exhumation, and deformation in the Chinese Tian Shan, *Geol. Soc. Am. Mem.* **194,** 71–99.

Farr, T. G., P. A. Rosen, E. Caro, R. Crippen, R. Duren, S. Hensley, and D. Seal (2007). The Shuttle Radar Topography Mission, *Rev. Geophys.* **45,** no. 2, 1–33, doi: 10.1029/2005RG000183.

Freed, A. M. (2005). Earthquake triggering by static, dynamic, and postseismic stress transfer, *Annu. Rev. Earth Planet. Sci.* **33,** 335–367, doi: 10.1146/annurev.earth.33.092203.122505.

Guan, S. W., B. L. Li, D. F. He, H. S. John, and Z. X. Chen (2009). Recognition and exploration of structural wedges—A case study of the southern margin of Junggar basin, *Earth Sci. Front.* **16,** no. 3, 129–137 (in Chinese).

Guan, S. W., C. J. Zhang, D. F. He, X. Shi, S. John, X. Wang, and X. Z. Wu (2006). Complex structural analysis and modeling: the first row of anticlinal belt on the southern margin of the Junggar basin, *Acta Geol. Sin.* **80,** no. 8, 1131–1140 (in Chinese).

Guzofski, C. A., J. H. Shaw, G. Lin, and P. M. Shearer (2007). Seismically active wedge structure beneath the Coalinga anticline, San Joaquin basin, California, *J. Geophys. Res.* **112,** B03S05, doi: 10.1029/2006JB004465.

Huang, M.-H., H. Tung, E. J. Fielding, H.-H. Huang, C. Liang, C. Huang, and J.-C. Hu (2016). Multiple fault slip triggered above the 2016 M_w 6.4 MeiNong earthquake in Taiwan, *Geophys. Res. Lett.* **43,** no. 14, 7459–7467, doi: 10.1002/2016GL069351.

Ishibe, T., Y. Ogata, H. Tsuruoka, and K. Satake (2017). Testing the Coulomb stress triggering hypothesis for three recent megathrust earthquakes, *Geosci. Lett.* **4,** no. 5, 1–11, doi: 10.1186/s40562-017-0070-y.

Johnson, K. M., and P. Segall (2004). Imaging the ramp-décollement geometry of the Chelungpu fault using coseismic GPS displacements from the 1999 Chi-Chi, Taiwan earthquake, *Tectonophysics* **378,** 123–139, doi: 10.1016/j.tecto.2003.10.020.

Kao, H., and W.-P. Chen (2000). The Chi-Chi earthquake sequence: Active out-of-sequence thrust faulting in Taiwan, *Science* **288,** 2346–2349, doi: 10.1126/science.288.5475.2346.

King, G. C. P., and C. Vita-Finzi (1981). Active folding in the Algerian earthquake of 10 October 1980, *Nature* **292,** no. 5818, 22–26.

Liu, G., X. Qiao, W. Xiong, Y. Zhou, Z. Nie, and C. Xia (2017). Source models for the 2016 M_w 6.0 Hutubi earthquake, Xinjiang, China: A possible reverse event, *Geodes. Geodyn.* **8,** no. 5, 311–318, doi: 10.1016/j.geog.2017.05.005.

Lu, R., D. He, X. Xu, X. Wang, X. Tan, and X. Wu (2018). Seismotectonics of the 2016 M 6.2 Hutubi earthquake: Implications for the 1906 M 7.7 Manas earthquake in the northern Tian Shan belt, China, *Seismol. Res. Lett.* **89,** no. 1, 13–21, doi: 10.1785/0220170123.

Lu, R., X. Xu, D. He, S. John, B. Liu, F. Wang, X. Tan, and Y. Li (2017). Seismotectonics of the 2013 Lushan M_w 6.7 earthquake: Inversion tectonics in the eastern margin of the Tibetan plateau, *Geophys. Res. Lett.* **44,** 8236–8243, doi: 10.1002/2017GL074296.

Nissen, E., J. R. Elliott, R. A. Sloan, T. J. Craig, G. J. Funning, A. Hutko, and T. J. Wright (2016). Limitations of rupture forecasting exposed by instantaneously triggered earthquake doublet, *Nature Geosci.* **9,** no. 4, 330–336.

Okada, Y. (1985). Surface deformation to shear and tensile fault in a half-space, *Bull. Seismol. Soc. Am.* **75,** no. 4, 1135–1154.

Shaw, J. H., C. Connors, and J. Suppe (2005). *Seismic Interpretation of Contractional Fault-Related Folds: An American Association of Petroleum Geologists Seismic Atlas*, Studies in Geology, Number 53, Am. Assoc. Petrol. Geol., Tulsa, Oklahoma.

Stein, R. S., and G. C. King (1984). Seismic potential revealed by surface folding: 1983 Coalinga, California, earthquake, *Science* **224,** 869–873.

Suppe, J. (1983). Geometry and kinematics of fault-bend folding, *Am. J. Sci.* **283,** no. 7, 684–721.

Suppe, J., C. D. Connors, and Y. K. Zhang (2004). Shear fault bend folding, in *Thrust Tectonics and Hydrocarbon Systems*, K. R. McClay (Editor), AAPG Memoir, Vol. 82**,** 303–323.

Wang, C. Y., Z. E. Yang, H. Luo, and W. D. Mooney (2004). Crustal structure of the northern margin of the eastern Tien Shan, China, and its tectonic implications for the 1906 M ∼ 7.7 Manas earthquake, *Earth Planet. Sci. Lett.* **223,** no. 1, 187–202, doi: 10.1016/j.epsl.2004.04.015.

Wang, H., M. Liu, J. Cao, X. Shen, and G. Zhang (2011). Slip rates and seismic moment deficits on major active faults in mainland China, *J. Geophys. Res.* **116,** no. B2, doi: 10.1029/2010JB007821.

Wang, Q., G. Ding, X. Qiao, X. Wang, and X. You (2000). Recent rapid shortening of crust across the Tianshan Mts. and relative motion of tectonic blocks in the north and south, *Chin. Sci. Bull.* **45,** no. 21, 1995–1999.

Wegnuller, U., C. Werner, T. Strozzi, A. Wiesmann, O. Frey, and M. Santoro (2016). Sentinel-1 support in the GAMMA Software, *Procedia Comput. Sci.* **100,** 1305–1312.

Welstead, S. T. (1999). *Fractal and Wavelet Image Compression Techniques*, SPIE Optical Engineering Press, Bellingham, Washington, 232 pp.

Wessel, P., and W. H. Smith (1998). New, improved version of Generic Mapping Tools released, *Eos Trans. AGU* **79,** no. 47, 579.

Xie, Y. S., and M. B. Cai (1986). *Collections of Historical Records of Earthquakes in China*, Science Press, Beijing, China (in Chinese).

Yang, X. P., Q. D. Deng, P. Z. Zhang, X. W. Xu, and G. H. Yu (1998). Active reverse fault-fold zones and estimation of potential earthquake sources in northern Tianshan, *Seismol. Geol.* **20,** no. 3, 193–200 (in Chinese).

Yang, Y.-H., Q. Chen, Q. Xu, G. Liu, and J.-C. Hu (2018). Source model and Coulomb stress change of the 2015 M_w 7.8 Gorkha earthquake determined from improved inversion of geodetic surface deformation observations, *J. Geodes.* 1–19, doi: 10.1007/s00190-018-1164-9.

Yang, Y.-H., Q. Chen, Q. Xu, Y. Zhang, Q. Yong, and G. Liu (2017). Coseismic surface deformation of the 2014 Napa earthquake mapped by Sentinel-1A SAR and accuracy assessment with COSMO-SkyMed and GPS data as cross validation, *Int. J. Digit. Earth* **10,** no. 12, 1197–1213, doi: 10.1080/17538947.2017.1299806.

Yang, Y.-H., M.-C. Tsai, J.-C. Hu, M. A. Aurelio, M. Hashimoto, J. A. P. Escudero, Z. Su, and Q. Chen (2018). Coseismic slip deficit of the 2017 M_w 6.5 Ormoc earthquake that occurred along a creeping segment and geothermal field of the Philippine fault, *Geophys. Res. Lett.* **45,** no. 6, 2659–2668, doi: 10.1002/2017GL076417.

Yin, A. (2010). Cenozoic tectonic evolution of Asia: A preliminary synthesis, *Tectonophysics* **488,** no. 1, 293–325, doi: 10.1016/j.tecto.2009.06.002.

Yin, A., S. Nie, P. Craig, T. M. Harrison, F. J. Ryerson, X. L. Qian, and G. Yang (1998). Late Cenozoic tectonic evolution of the southern Chinese Tian Shan, *Tectonics* **7,** no. 1, 1–27.

Zhang, P. Z., Q. D. Deng, S. Z. Peng, and X. P. Yang (1994). Blind thrust, folding earthquake, and the 1906 Manas earthquake, Xinjiang, *Seismol. Geol.* **16,** no. 3, 193–204 (in Chinese).

Zhou, W. X., Z. E. Yang, J. X. Sun, and R. B. Zhao (2003). Numerical modeling of the generation process of the 1906 Manas M_s 7.7 earthquake, *Seismol. Geol.* **25,** no. 4, 609–616.

Department of Remote Sensing and Surveying Engineering
Southwest Petroleum University
Chengdu 610500, People's Republic of China
xzhfhyyy@126.com
zegen01@126.com
(Y.-H.Y., Z.-G.W.)

Department of Geosciences
National Taiwan University
Taipei 10617, Taiwan, R.O.C.
jchu@ntu.edu.tw
(J.-C.H.)

Seismological Center
Central Weather Bureau
Taipei 10048, Taiwan, R.O.C.
minchyen@scman.cwb.gov.tw
(M.-C.T.)

Department of Remote Sensing and Geoinformation Engineering
Southwest Jiaotong University
Chengdu 610031, People's Republic of China
swjtucq@sina.com
(Q.C.)

Manuscript received 17 May 2018;
Published Online 29 January 2019